Supplementary Information for

Anion-π Interaction and Solvent Dehydrogenation Control Enable High-Voltage Lithium-ion Batteries

Tao Zhou[1#], Jinze Wang[1#], Ling Lv[1#], Ruhong Li[1,2*], Long Chen[1], Shuoqing Zhang[1,3], Haikuo Zhang[1], Baochen Ma[1], Jiajie Huang[1], Bing Wu[4], Lixin Chen[1], Tao Deng[3*], Xiulin Fan[1*]

1. State Key Laboratory of Silicon and Advanced Semiconductor Materials, School of Materials Science and Engineering, Zhejiang University, Hangzhou 310027, China.

2. ZJU-Hangzhou Global Scientific and Technological Innovation Center, Zhejiang University, Hangzhou 311215, China

3. China-UK Low Carbon College, Shanghai Jiao Tong University, Shanghai 201306, China

4. Institute of Emergency Science, Chinese Institute of Coal Science (CICS), Beijing 1000013, China

Tao Zhou, Jinze Wang, and Ling Lv contributed equally to this paper.

*Corresponding Author: ruhong@zju.edu.cn, taodeng@sjtu.edu.cn, xlfan@zju.edu.cn

1. Supplementary Methods

Preparation of electrolyte

Benzonitrile (BN), 4-fluorobenzonitrile (FBN), 1,4-dicyanobenzene (DBN), 3,5-dicyanofluorobenzene (DFBN), 3-(trifluoromethyl)benzonitrile (TFBN), 3,5-bis(trifluoromethyl)benzonitrile (BFBN), 2-fluoro-4-(trifluoromethyl)benzonitrile (FTFBN) , and 1,3,6-hexanetricarbonitrile (HTCN) were purchased from Aladdin and used as received. Battery-grade lithium hexafluorophosphate ($LiPF_6$), lithium bis(fluorosulfonyl)imide (LiFSI), ethylene carbonate (EC), ethyl methyl carbonate (EMC), diethyl carbonate (DEC), and fluoroethylene carbonate (FEC) were obtained from Changde Dadu New Material Co., Ltd. EMC and DEC were dried with 4 Å molecular sieves (Sigma-Aldrich) before use. 1 M $LiPF_6$ in EC/EMC/DEC (1:1:1, v/v) +5 wt.% FEC was defined as the baseline electrolyte (BE). Additives-containing electrolytes were fabricated by adding various additives into BE with a mass percentage of 1%. All electrolytes were prepared in an Argon-filled glove box with O_2 and H_2O levels <0.01 ppm.

Cell assembly and electrochemical measurements

The Gr||LCO pouch cells (1.0 and 1.5 Ah) were provided by Li-FUN Technology Co., Ltd. For the 1.0 Ah pouch cell, the mass loading of cathode electrode is 13.6 mg cm^{-2} with a 98.6% active material ratio, while the mass loading of anode electrode is 8.75 mg cm^{-2} with a 97.3% active material ratio. The 1.0 Ah pouch cell contains 9 cathode layers. For the 1.5 Ah pouch cell, the mass loading of cathode electrode is 12.01 mg cm^{-2} with a 97.2% active material ratio, while the mass loading of anode electrode is 7.72 mg cm^{-2} with a 96.7% active material ratio. The 1.5 Ah pouch cell contains 13 cathode layers. The pouch cells were injected with 3 g Ah^{-1} electrolytes before sealing. The charge/discharge tests, galvanostatic intermittent titration technique (GITT) tests, rate tests and electrochemical impedance spectroscopy (EIS) tests were all conducted on Gr||LCO pouch cells. For the charge/discharge tests, pouch cells were activated at a rate of 0.1 C for the initial two cycles and then operated at 0.5 C for long-term

cycling with a cutoff voltage between 4.55 V and 3.0 V using a LAND battery testing system (Wuhan LAND Electronics Co., Ltd.). In GITT tests, cells were cycled at a rate of C/3 with 12 min pulse time and 5 h rest time (after 100 cycles of 0.5 C charge/discharge). During the rate test, cells were discharged at 0.1 C, 0.2 C, 0.5 C, 0.7 C, 1.0 C, 1.2 C, 1.5 C and 2.0 C with the same charge rate of 0.2 C and back to 0.1 C for long-term cycling. EIS measurements of the Gr||LCO full cells at a fully discharged state were performed using an Chi660E electrochemical workstation (Chenhua, Shanghai) over frequencies from 10^6 Hz to 10^{-2} Hz.

Materials characterizations

X-ray photoelectron spectroscopy (XPS) spectra were obtained by a Thermo Scientific K-Alpha with an Al Ka X-ray source of 1486.6 eV. Time-of-flight secondary ion mass spectroscopy (TOF-SIMS) measurements were conducted with an ION-TOF TOF.SIMS5 spectrometer. Before the XPS and TOF-SIMS tests, the cathodes were disassembled from Gr||LCO pouch cells after 100 cycles and rinsed three times with anhydrous dimethyl carbonate (DMC) to remove the residuals. For differential scanning calorimetry (DSC) tests, the cathode materials (approximately 10 mg) were collected from 4.55 V-fully-charged Gr||LCO pouch cells to obtain hybrid with 10 μL electrolyte. The hybrids were conducted on the DSC Q2000 V24.11 Build 124 from ambient to 400 °C at a heating rate of 5 °C min^{-1}. Scanning electron microscope (SEM, Hitachi SU-70) and high-resolution transmission electron microscopy (HRTEM, Hitachi SU-70) were performed to gain the morphology and microstructure information. Focused ion beam (FIB, FEI Scios) was carried out to prepare LCO slices for inner morphology observation. X-ray diffraction (XRD, X-pert Powder, PANalytical B.V.) experiment was used with Cu Kα radiation from 5° to 80° at a scanning speed of 4° min^{-1}. *Ex situ* Fourier transform infrared (FTIR) experiment was performed with a Thermo Scientific Nicolet iS20 instrument. The interaction between PF_6^- and BFBN was detected by ^{19}F nuclear magnetic resonance spectroscopy (NMR, Germany Bruker 600MHz). For the inductive coupled plasma optical emission spectrometer (ICP-OES) characterizations, the fully-discharged-state Gr anodes disassembled from Gr||LCO pouch cells were directly removed into

Agilent 720ES instrument to quantify the Co content. To identify Co concentration in the electrolyte, the fully-charged-stated LCO electrode (70 mg) was soaked in the electrolyte (10 mL) for 7 days, and then the electrolyte was taken for ICP testing.

***In situ* FTIR measurement**

A Thermo Nicolet 8700 spectrometer equipped with an MCT detector cooled by liquid nitrogen was utilized for *in situ* electrochemical infrared reflection absorption spectroscopy (IRAS) measurements. A trapezoidal CaF_2 optical window was employed, and the incident angle of infrared light was set at 60°. The prepared catalyst was sandwiched between a meticulously cleaned glassy carbon electrode, polished with alumina and subjected to ultrasound cleaning, and the optical window. Infrared light underwent reflection at the CaF_2 and liquid interface, giving rise to evanescent waves for the detection of solution-phase information. The distance between the glassy carbon electrode and the window was controlled within the range of 10 to 30 μm. It is important to note that strict control of the liquid layer thickness was maintained to ensure a sufficiently high signal-to-noise ratio in the infrared spectrum.

Subsequently, testing was conducted in a homemade *in situ* cell, with Hg/HgO used as a reference. The reference electrode was introduced near the working electrode *via* a Luggin capillary, and Li foil served as the counter electrode. The working electrode was prepared by casting the slurry consisting of 90 wt.% LCO, 5 wt.% Super P, and 5 wt.% polyvinylidene fluoride in N-methyl-2-pyrrolidone onto silicon crystal. All spectra were presented as $\Delta R/R=(E_s-E_R)/E_R$, where E_s and E_R represent the sample and reference spectra, respectively.

Computational methods

Gaussian 16 software was implemented to optimize molecular geometries of ground state with m062x/def2TZVP method and the GD3 dispersion model[1]. The interaction energy of additives and EC or PF_6^- (E_{sol} or E_{anion}) was defined as follow equations:

$$E_{sol} = E_{adv\text{-}EC} - E_{adv} - E_{EC} \tag{1}$$

$$E_{anion} = E_{adv\text{-}PF_6^-} - E_{adv} - E_{PF_6^-}$$

(2)

where $E_{adv\text{-}EC}$, $E_{adv\text{-}PF_6^-}$, E_{adv}, E_{EC}, and $E_{PF_6^-}$ represent the energy of additive and EC cluster, additive and PF_6^- cluster, additive, EC, PF_6^-, respectively.

In SMD solvation model, the molecules were positioned in the implicit solvent environment with $\varepsilon = 20.5$. Reduction potential E_{red} of different solvents paired with Li^+ was calculated from the equations[2]:

$$E_{red} = \left[\Delta G_{sol}(M) - \Delta G_{sol}(M^-) - \Delta G_g^{red}\right]/nF - 1.44$$

(3)

where ΔG_g^{red} are the free energy of reduction of molecule M in the gas phase at 298.15 K; $\Delta G_{sol}(M^-)$ and $\Delta G_{sol}(M)$ are the free energies of solvation of the reduced and initial complexes, respectively; n is the number of electrons involved in reduction reaction; F is the Faraday constant.

The electrostatic potential of BFBN, HTCN, EC and PF_6^- was calculated by Multiwfn program[3] and visualized through Visual Molecular Dynamics (VMD) program.

Independent gradient model based on Hirshfeld partition (IGMH)[4] was calculated by Multiwfn program[3] and used to visual analysis of interactions between additives and EC or PF_6^-. The FT-IR spectra were simulated by computing the vibrational frequencies of solvent molecules and solvent-ions complexes.

To explore the effects of additives on the cathode surface, Ab initio molecular dynamics (AIMD) and adsorption energy calculations were carried out using the Vienna Ab initio Simulation Package[5-7]. The projector augmented wave (PAW) method was used accompanied with the Perdew-Burke-Ernzerhof (PBE) exchange-correlation functional in the Generalized Gradient Approximation (GGA). The (104) surface of $LiCoO_2$ was cleaved and a slab model $LiCoO_2$ was created and optimized until the energy and force were less than 1×10^{-5} eV and 0.01 eV Å^{-1}, respectively. DFT+U method was employed and $U_{eff} = U\text{-}J = 3.3$ eV was applied on the transition metal d states[8]. The electrolytes models were constructed using Moltemplate (http://www.moltemplate.org/) and simulated in the NVT ensemble using a Nosé-

Hoover thermostat. Before building the interface models, the electrolytes were simulated for 5 ps to obtain stable structures. After that, the interface models were built with slab models (with or without BFBN) and electrolytes, simulations were performed for 5 ps to study the movement of PF_6^- relative to the interface. The adsorption energy of additives on the $LiCoO_2$ surface (ΔE_{ads}) was calculated based on the following equation:

$$\Delta E_{ads} = E_{adv\text{-}surface} - E_{adv} - E_{surface} \tag{4}$$

where $E_{adv\text{-}surface}$, E_{adv} and $E_{surface}$ represent the energy of structure with additive adsorbed on surface, additive and surface, respectively.

2. Supplementary Figures
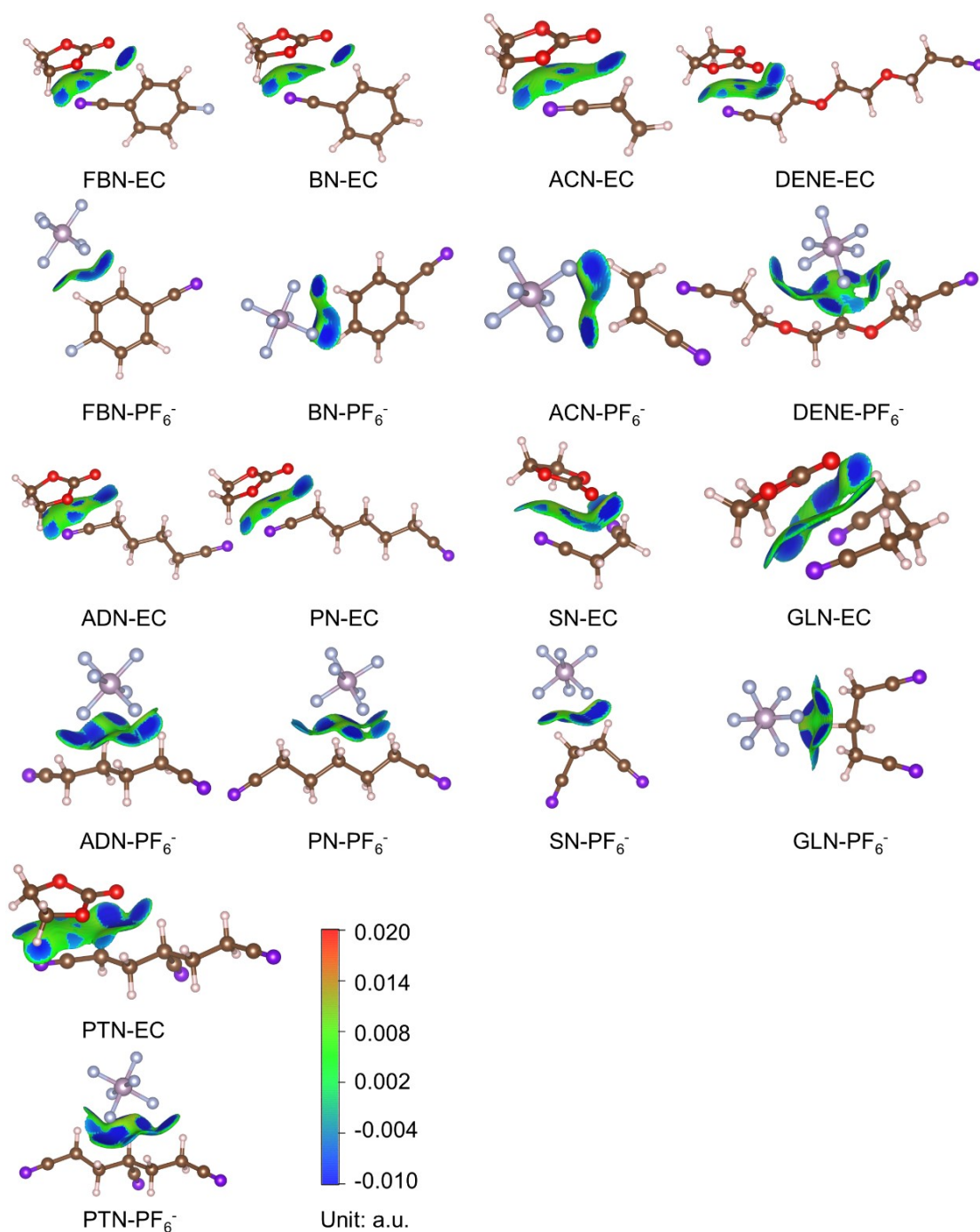
Figure S1. Sign($\lambda 2$)ρ colored isosurfaces of $\delta g^{inter} = 0.005$ a.u. corresponding to IGMH analyses for FBN-EC, FBN-PF$_6^-$, BN-EC, BN-PF$_6^-$, ACN-EC, ACN-PF$_6^-$, DENE-EC, DENE-PF$_6^-$, ADN-EC, ADN-PF$_6^-$, PN-EC, PN-PF$_6^-$, SN-EC, SN-PF$_6^-$, GLN-EC, GLN-PF$_6^-$, PTN-EC and PTN-PF$_6^-$ complexes. The blue, green and red on isosurfaces represent the attractive interaction, van der Waals interaction and

repulsive interaction between molecules, respectively. Color code: silver, H; brown, C; red, O; purple, N; cyan, F; pink, P.

Two phenyl-substituted nitriles (FBN and BN) and linear nitriles (ACN, DENE, ADN, PN, SN, GLN and PTN) listed above interact with EC and PF_6^- mainly through H atoms. BN and FBN are counterexamples to phenyl-substituted nitriles, where they interact with the anion *via* H atom rather than π-stacking. This can be explained by the lower positivity of the π-stacking due to the fewer electron-withdrawing substituents on the phenyl group.

Figure S2. Sign(λ2)ρ colored isosurfaces of δg^{inter} = 0.005 a.u. corresponding to IGMH analyses for TFBN-EC, TFBN-PF$_6^-$, DBN-EC, DBN-PF$_6^-$, DFBN-EC, DFBN-PF$_6^-$, FTFBN-EC and FTFBN-PF$_6^-$ complexes. The blue, green and red on isosurfaces represent the attractive interaction, van der Waals interaction and repulsive interaction between molecules, respectively. Color code: silver, H; brown, C; red, O; purple, N; cyan, F; pink, P.

The phenyl-substituted nitriles listed above (TFBN, DBN, DFBN and FTFBN) interact with EC through H atoms and interact with PF$_6^-$ through π-stacking of the phenyl group.
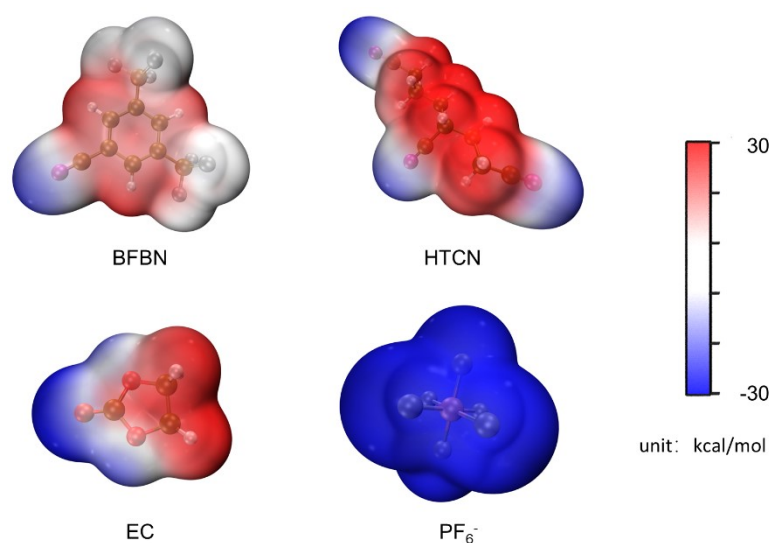
Figure S3. The electrostatic potential (ESP) calculations of BFBN, HTCN, EC and PF$_6^-$.

To gain a further understanding of the interaction sites of nitrile-EC and nitrile-PF$_6^-$ complexes, the ESP of BFBN, HTCN, EC and PF$_6^-$ (BFBN and HTCN are representatives of phenyl-substituted and linear nitriles, respectively) were calculated. The carbonyl oxygen of EC possesses negative ESP and therefore results in interactions with H atoms (positive ESP) of BFBN and HTCN. For BFBN, owing to the strong electron-withdrawing and steric hindrance effects of -CN and -CF$_3$ groups, the phenyl possesses positive ESP and exhibits a priority to interact with the anion PF$_6^-$. In contrast, HTCN does not have such similar effects and thus interacts with PF$_6^-$ *via* H atoms.
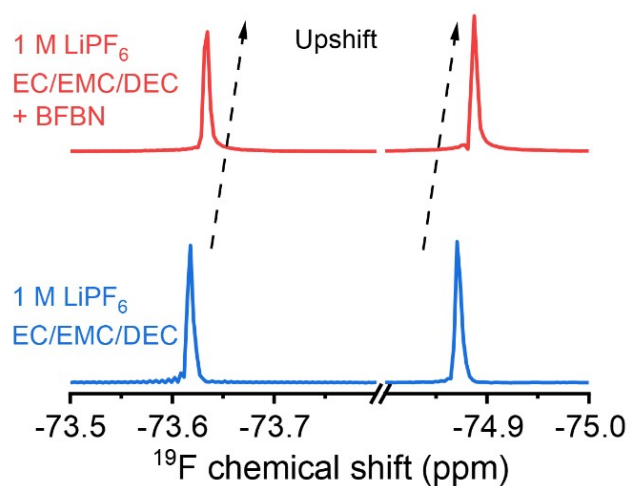
Figure S4. ^{19}F NMR results of PF_6^- in different electrolytes.

The NMR experiments were carried out using an internal NMR insert[9] with 0.1 M LiFSI in 1 vol.% H_2O + 10 vol.% C_2H_5OH + 98 vol.% D_2O as the reference. All the ^{19}F spectra were referenced to the ^{19}F signal of LiFSI at 51.85 ppm.
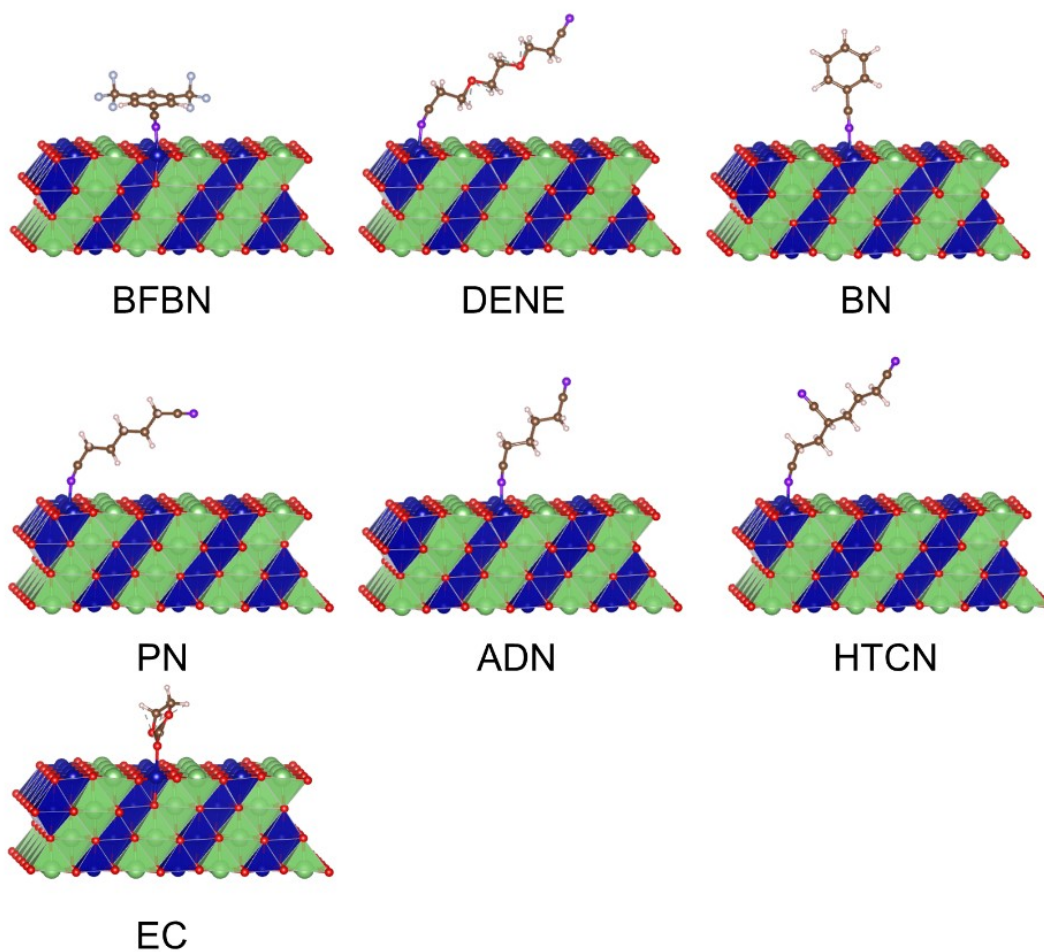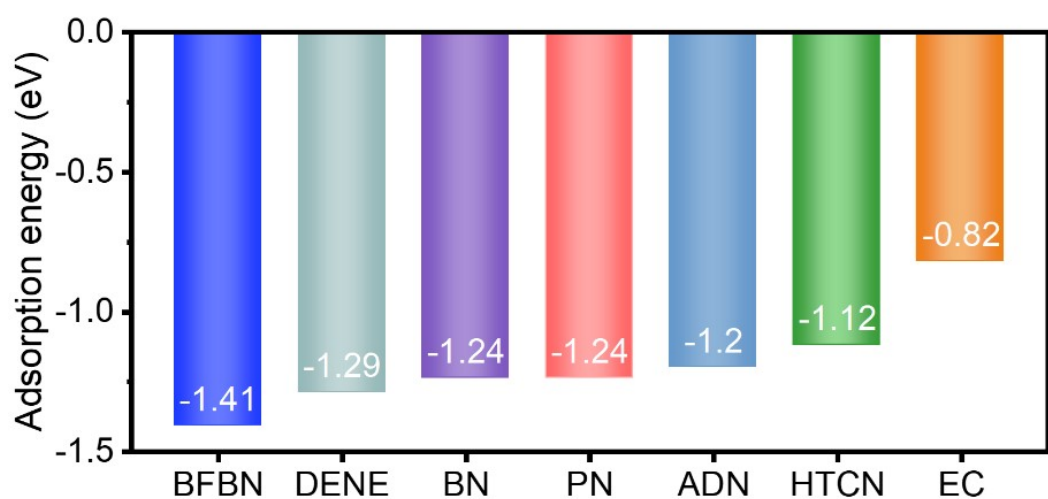
Figure S5. Adsorption energy of BFBN, DENE, BN, PN, ADN, HTCN and EC on LCO surface and corresponding structures. Color code: pink, H; brown, C; red, O; purple, N; cyan, F; deep pink, P; dark blue, Co; green, Li.
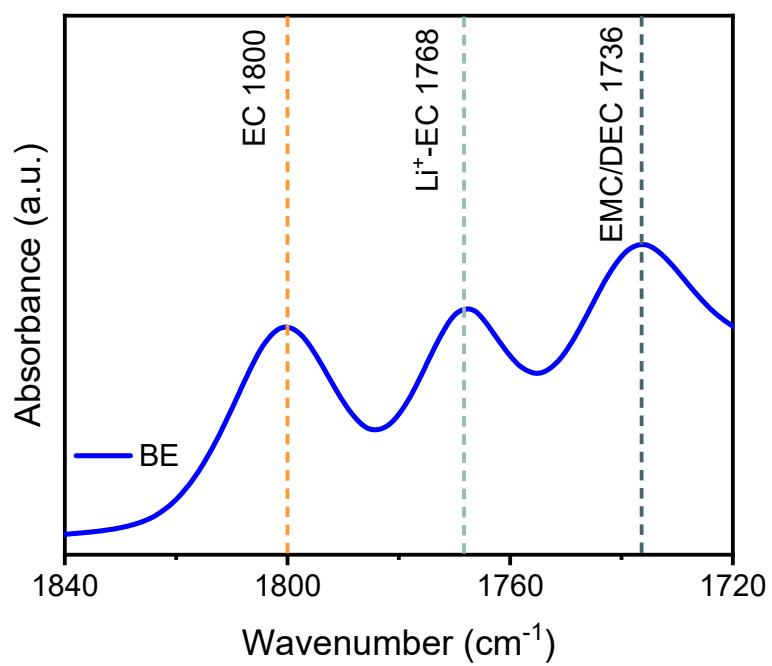
Figure S6. Attenuated total reflectance (ATR) measurement of the BE electrolyte in the C=O stretching region, where the assignment of spectroscopic features was labeled on each peak.
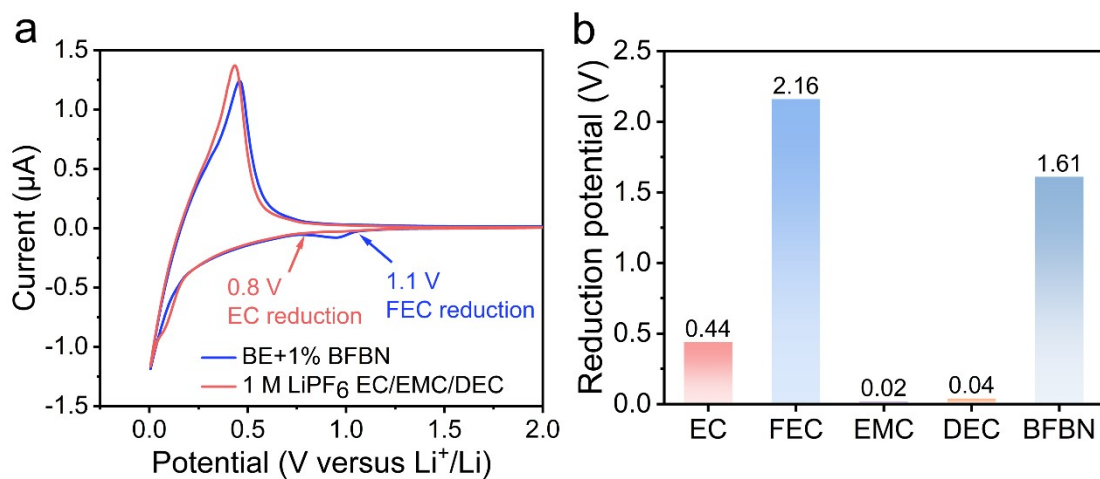
Figure S7. Electrolyte reduction stability measurement. a) CV curves of Li‖Gr half cells with different electrolytes at a scanning rate of 0.5 mV s^{-1}. b) Reduction potential calculation of BFBN and various solvents.
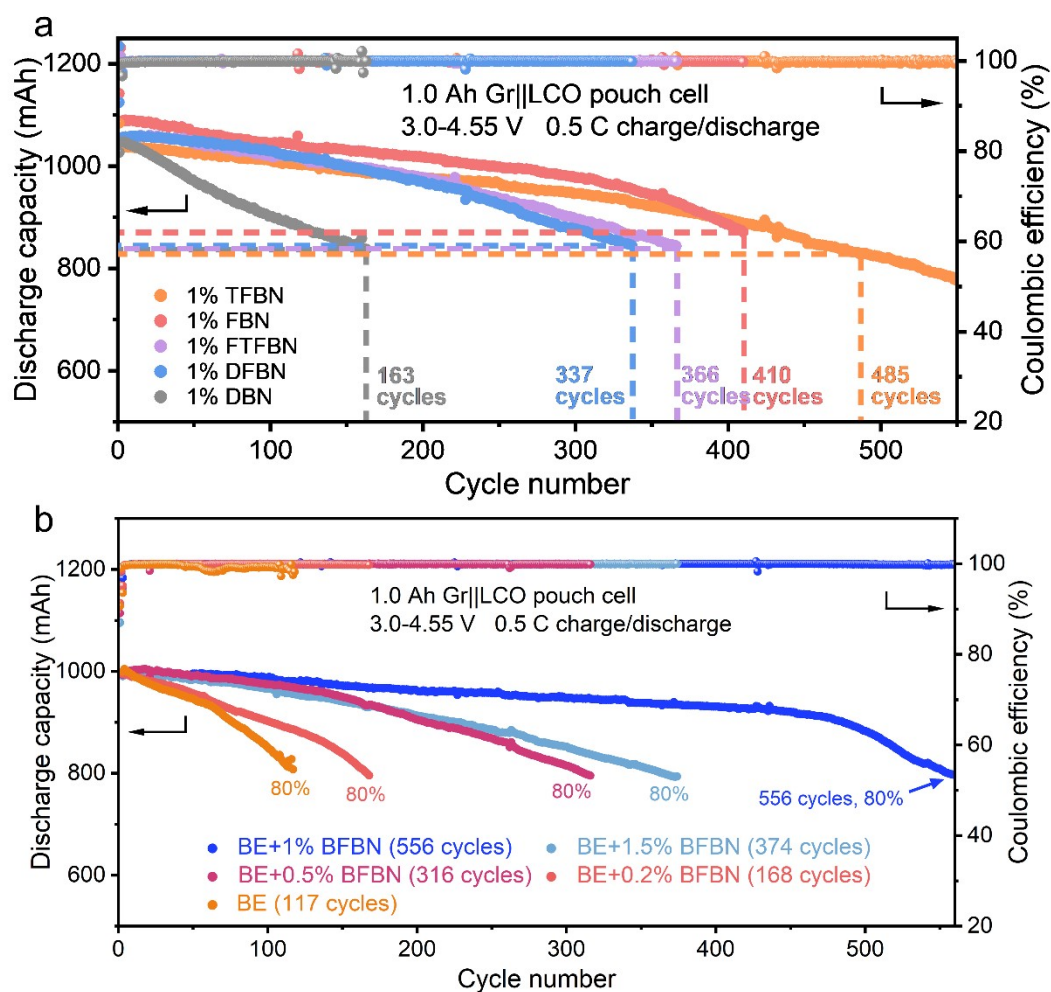
Figure S8. Cycling performance of Gr||LCO pouch cells with a) different additives and b) different amounts of BFBN at 25 °C. With 80 % of capacity retention as the threshold, the life span of pouch cells with various additives was labeled in the figure.

Comparative experiments with varying amounts of BFBN identified 1% as the optimal amount concentration. The poor cycling performance observed with 0.2% and 0.5% addition is likely due to the insufficient protection on the LCO cathode. Pouch cell with 1.5% BFBN exhibits shorter cycle life compared to the 1% addition, as the excess nitrile content likely counteracted the protective effect of FEC on graphite.
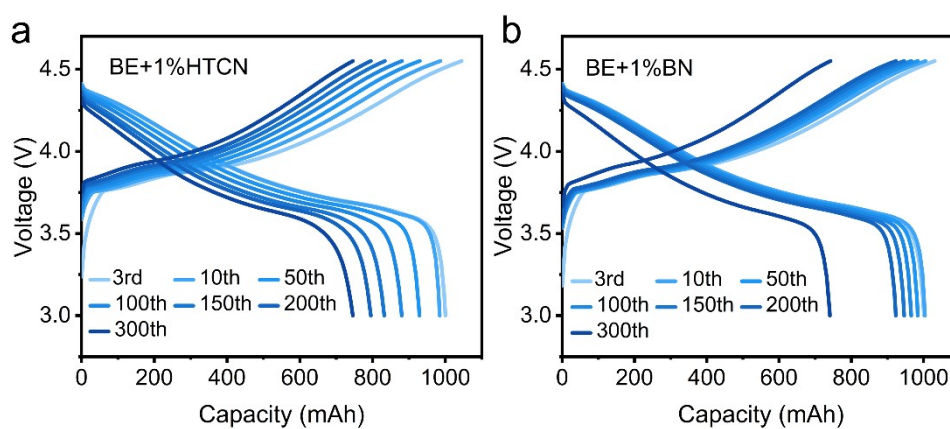
Figure S9. Typical charge/discharge curves of 1.0 Ah Gr‖LCO pouch cells with the a) BE+1% HTCN and b) BE+1% BN electrolytes at 25 °C.
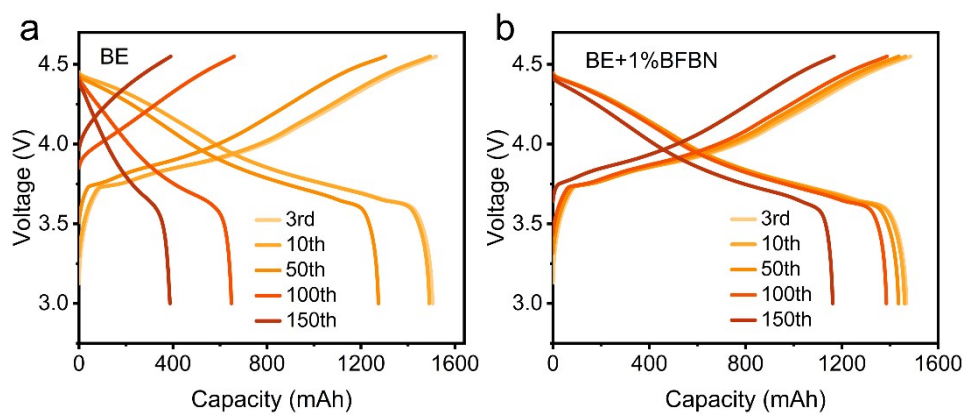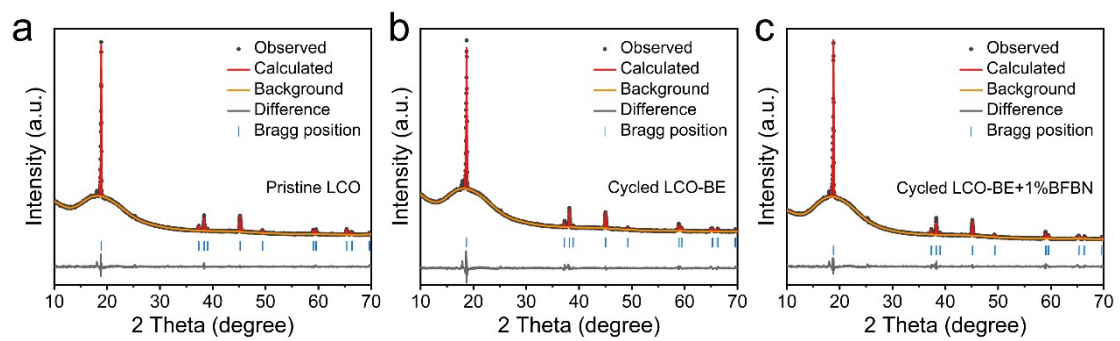
Figure S10. Typical charge/discharge curves of 1.5 Ah Gr‖LCO pouch cells with the a) BE and b) BE+1% BFBN electrolytes at 45 °C.
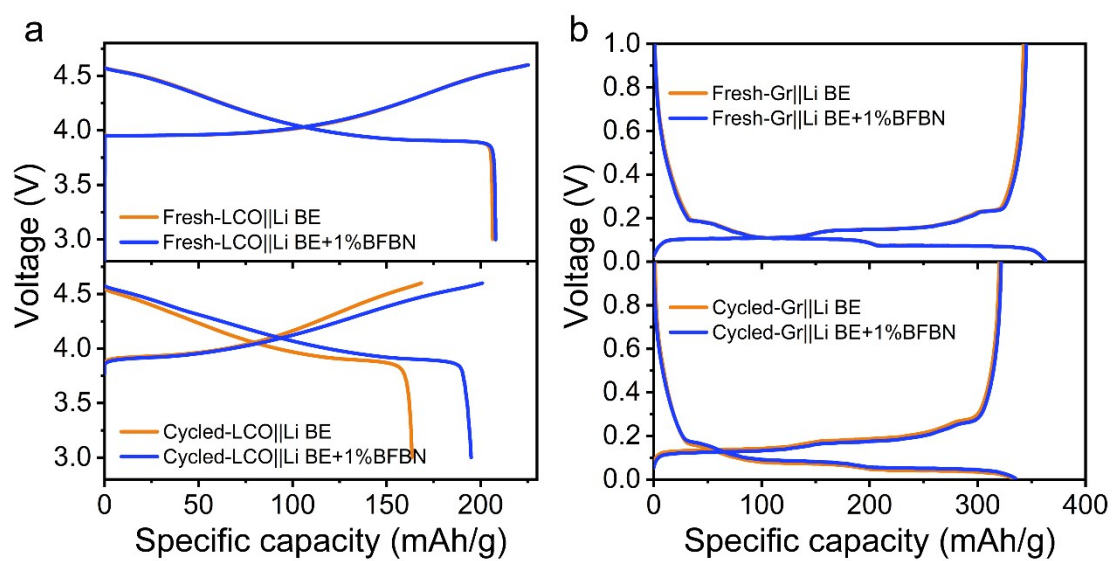
Figure S11. Reversible capacity evaluation of LCO and Gr electrodes. a) Voltage profiles of LCO‖Li coin cells between 3.0 V and 4.6 V with different electrolytes. b) Voltage profiles of Gr‖Li coin cells between 0.005 V and 1.0 V with different electrolytes.

Figure S12. The XRD and Rietveld refinement pattern of a) pristine LCO, b) LCO cycled with BE and c) LCO cycled with BE+1% BFBN.
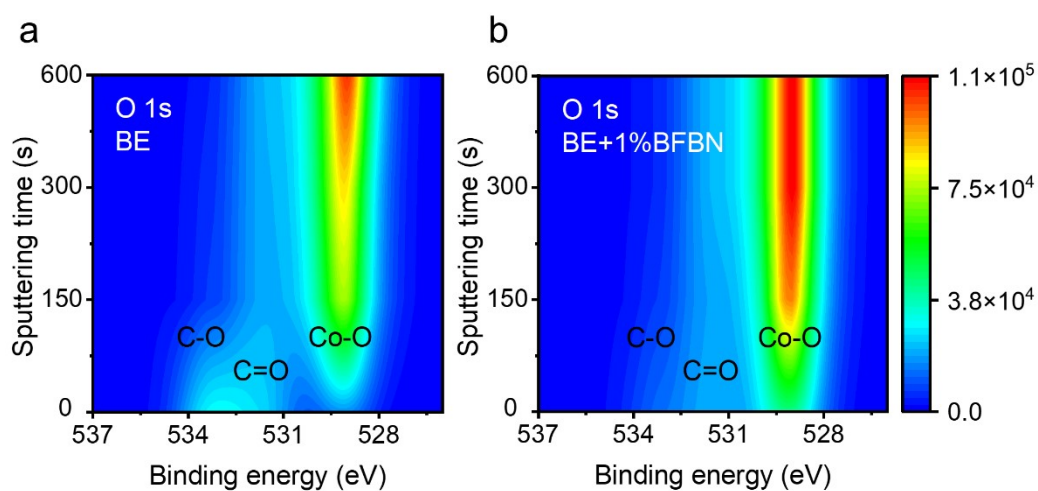
Figure S13. XPS O 1s spectra of LCO cathodes recovered from Gr||LCO pouch cells after 100 cycles in a) BE and b) BE+1% BFBN electrolytes.
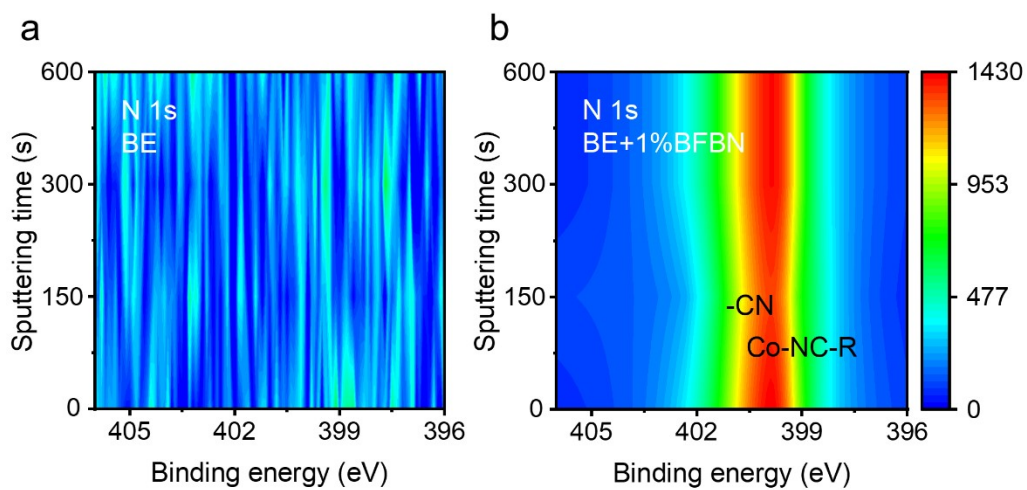
Figure S14. XPS N 1s spectra of LCO cathodes recovered from Gr||LCO pouch cells after 100 cycles in a) BE and b) BE+1% BFBN electrolytes
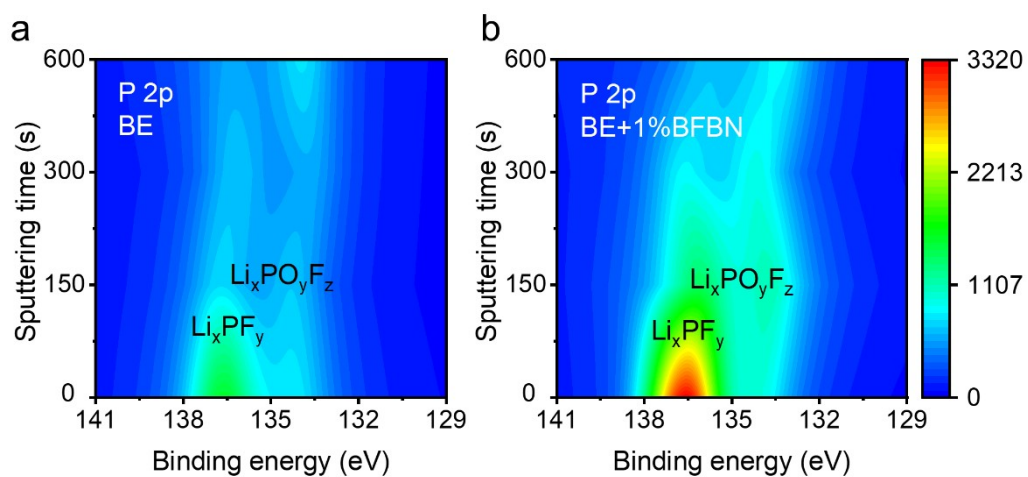
Figure S15. XPS P 2p spectra of LCO cathodes recovered from Gr‖LCO pouch cells after 100 cycles in a) BE and b) BE+1% BFBN electrolytes.
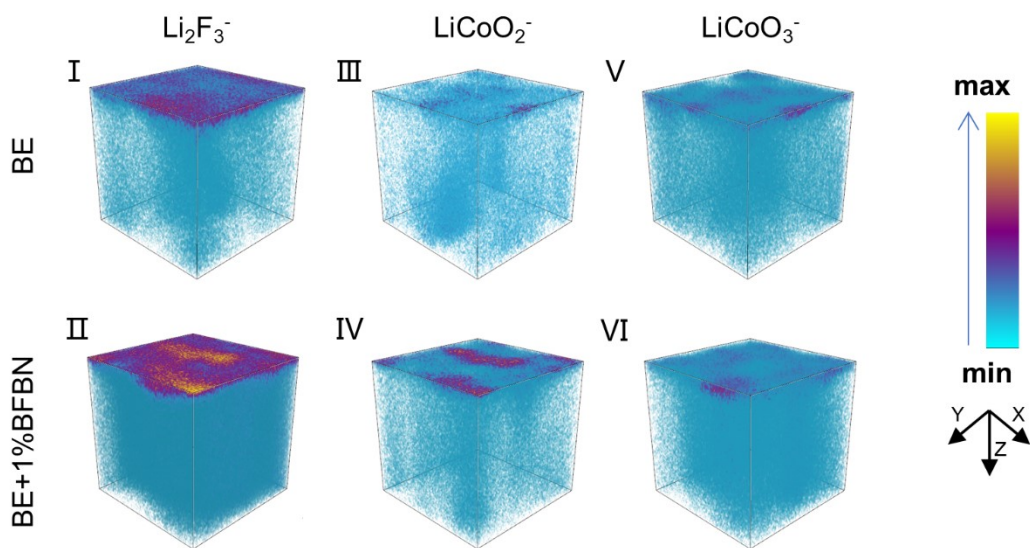
Figure S16. 3D-rendering images of $Li_2F_3^-$ (I and II), $LiCoO_2^-$ (III and IV), and $LiCoO_3^-$ (V and VI) species on the LCO cathode interface cycled in BE and BE+1% BFBN electrolytes.
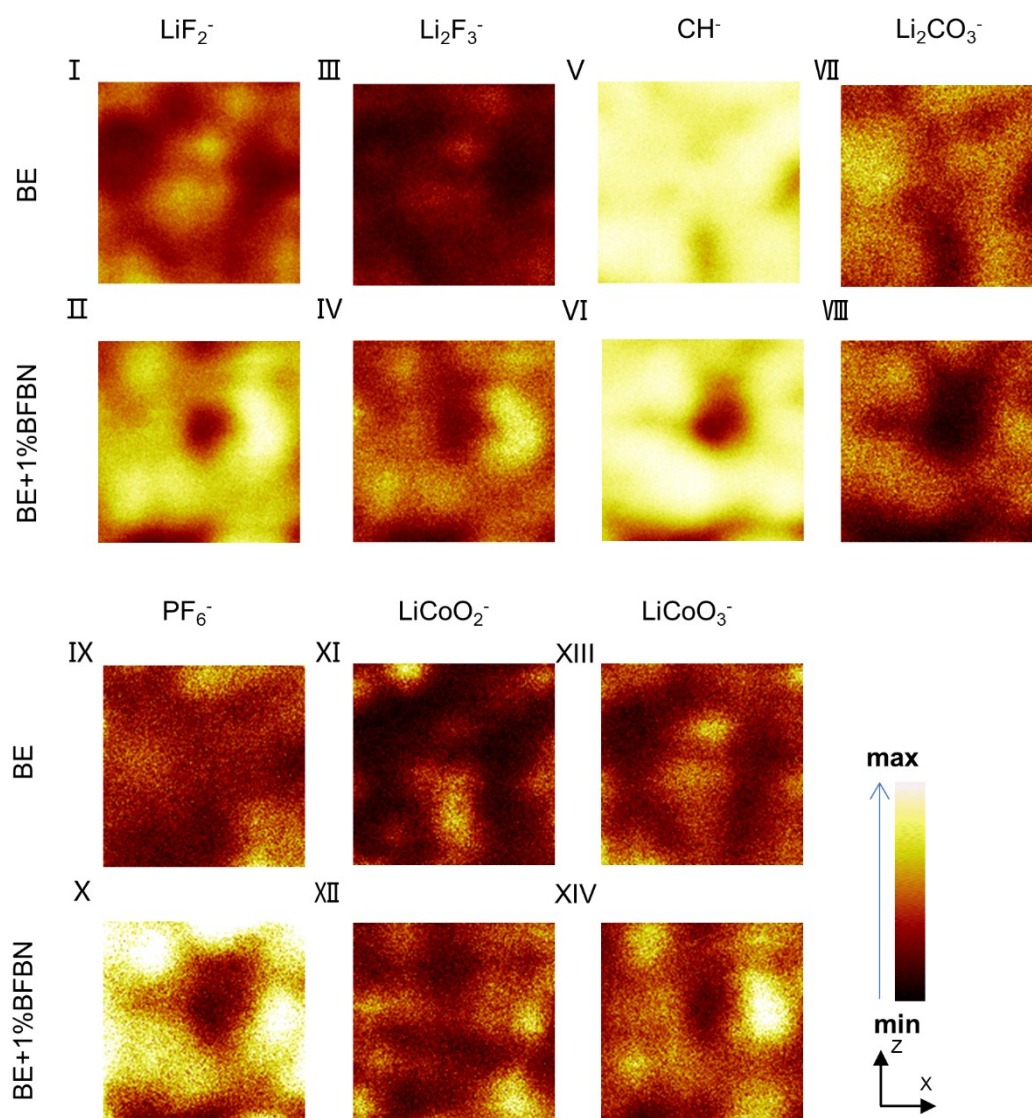
Figure S17. The intuitive XZ-2D plane reconstructed images of LiF_2^- (I and II), $Li_2F_3^-$ (III and IV), CH^- (V and VI), $Li_2CO_3^-$ (VII and VIII), PF_6^- (IX and X), $LiCoO_2^-$ (XI and XII), and $LiCoO_3^-$ (XIII and XIV) species on the LCO cathode interface cycled in BE and BE+1% BFBN electrolytes. Size: 50μm × 50μm.
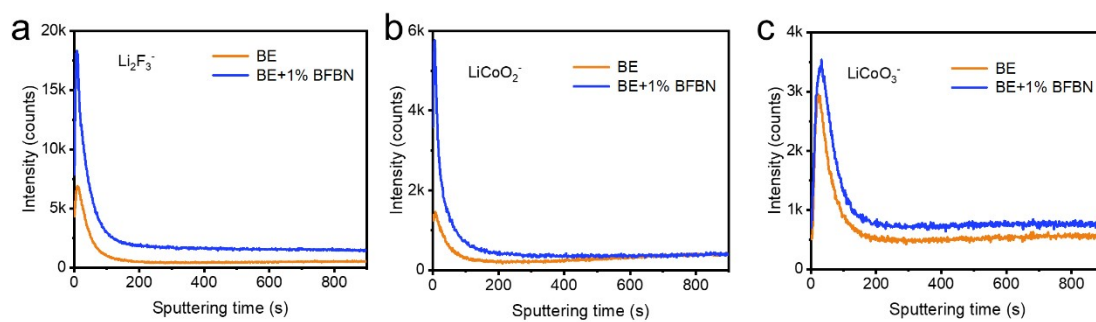
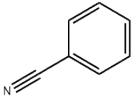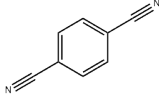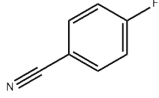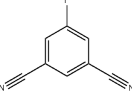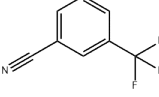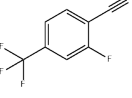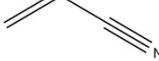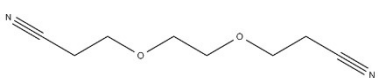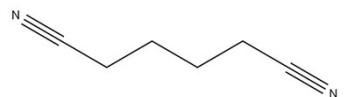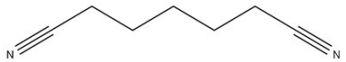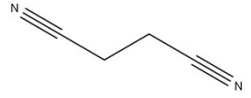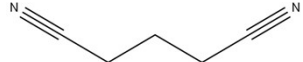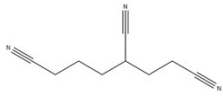**Figure S18**. TOF-SIMS intensity depth profiles of a) $Li_2F_3^-$, b) $LiCoO_2^-$ and c) $LiCoO_3^-$ fragments on LCO cathode surface after cycling in BE and BE+1% BFBN electrolytes.

3. Supplementary Tables

Supplementary Table S1. Summary of all nitrile additives in Figure 1a.

Abbreviations	Name	Molecular formula
BN	Benzonitrile	
DBN	1,4-Dicyanobenzene	
FBN	4-Fluorobenzonitrile	
BFBN	3,5-Bis(trifluoromethyl)benzonitrile	
DFBN	3,5-Dicyanofluorobenzene	
TFBN	3-(Trifluoromethyl)benzonitrile	
FTFBN	2-Fluoro-4-(trifluoromethyl)benzonitrile	
ACN	Acrylonitrile	
DENE	Ethylene glycol bis(propionitrile) ether	
ADN	Adiponitrile	
PN	1,5-Dicyanopentane	
SN	Succinonitrile	
GLN	Glutaronitrile	
HTCN	1,3,6-Hexanetricarbonitrile	

| PTN | 1,3,5-Pentanetricarbonitrile | |
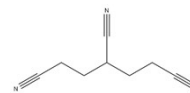
Supplementary Table S2 Interaction energies of various nitriles additives with EC and PF_6^- corresponding to Figure 1a.

Additives	Interaction energy with EC (kcal/mol)	Interaction energy with PF_6^- (kcal/mol)
BFBN	1.66039	-6.54116
BN	1.52485	-2.89596
TFBN	-0.1575	-0.52711
DBN	0.77058	-1.92394
DFBN	-0.13617	-3.65462
FBN	1.55999	-2.78614
FTFBN	0.90863	-2.53765
HTCN	-1.14583	-15.55722
ACN	1.37111	-3.22038
ADN	0.1801	-8.76129
DENE	0.93687	-7.51945
GLN	-1.19101	-10.66703
PN	0.30434	-9.52434
PTN	-1.78526	-16.53488
SN	0.31313	-11.23995

Supplementary Table S3. XRD Rietveld refinement results of pristine-LCO.

Pristine-LCO (Space Group R-3m)							
Atomic Occupancies	Atom	Wyckoff Position	x	y	z	Occ.	Uiso.
	Li	3b	0.0000	0.0000	0.5000	1.0000	0.19440
	Co	3a	0.0000	0.0000	0.0000	1.0000	0.16578
	O	6c	0.0000	0.0000	0.2258	1.0000	0.12462
Lattice Parameters	a (Å)	b (Å)	c (Å)	α	β	γ	c/a	$I_{(003)}/I_{(104)}$
	2.814	2.814	14.065	90°	90°	120°	4.9982	6.72
Agreement Factors							
χ^2=1.514			R_{wp}=1.60%			R_p=1.10%	

Supplementary Table S4. XRD Rietveld refinement results of LCO cycled with BE.

LCO cycled with BE (Space Group R-3m)							
Atomic Occupancies	Atom	Wyckoff Position	x	y	z	Occ.	Uiso.
	Li	3b	0.0000	0.0000	0.5000	0.9874	0.20076
	Co	3a	0.0000	0.0000	0.0000	0.9958	0.11586
	O	6c	0.0000	0.0000	0.2275	1.0000	0.12143
Lattice Parameters	a (Å)	b (Å)	c (Å)	α	β	γ	c/a	$I_{(003)}/I_{(104)}$
	2.816	2.816	14.055	90°	90°	120°	4.9911	6.38
Agreement Factors							
χ^2=3.088			R_{wp}=2.22%			R_p=1.32%	

Supplementary Table S5. XRD Rietveld refinement results of LCO cycled with BE+1%BFBN.

LCO cycled with BE+1%BFBN (Space Group R-3m)							
Atomic Occupancies	Atom	Wyckoff Position	x	y	z	Occ.	Uiso.
	Li	3b	0.0000	0.0000	0.5000	0.9932	0.70731
	Co	3a	0.0000	0.0000	0.0000	0.9991	0.07933
	O	6c	0.0000	0.0000	0.2294	1.0000	0.14290
Lattice Parameters	a (Å)	b (Å)	c (Å)	α	β	γ	c/a	$I_{(003)}/I_{(104)}$
	2.813	2.813	14.059	90°	90°	120°	4.9979	6.54
Agreement Factors							
χ^2=2.295			R_{wp}=1.86%			R_p=1.20%	

Supplementary Table S6 Fitted impedance values of Gr‖LCO pouch cells after specified cycles corresponding to Figure 4d and 4h.

Cycles	BE			BE+1% BFBN		
	R_{ct} (Ω)	R_{sf} (Ω)	R_b (Ω)	R_{ct} (Ω)	R_{sf} (Ω)	R_b (Ω)
2nd	0.03	0.0286	0.2714	0.027	0.027	0.268
50th	0.0375	0.0561	0.2739	0.024	0.031	0.273
100th	0.0525	0.0761	0.2764	0.03	0.0348	0.2752
150th	0.0644	0.09	0.2806	0.028	0.044	0.276
200th	0.106	0.119	0.285	0.031	0.044	0.28
250th	0.13	0.132	0.295	0.033	0.045	0.285

The axis intercept of Z' of Nyquist plots at high frequency refers to bulk electrolyte resistance (R_b) of the battery. The two depressed semicircles at high-to-medium frequency represent R_{sf} and R_{ct} respectively, in which the former means the surface film resistance, while the latter can be ascribed to the charge transfer resistance[10, 11].

Reference

1. S. Grimme, J. Antony, S. Ehrlich and H. Krieg, *J. Chem. Phys.*, 2010, **132**, 154104.
2. D. Wang, T. He, A. Wang, K. Guo, M. Avdeev, C. Ouyang, L. Chen and S. Shi, *Adv. Funct. Mater.*, 2023, **33**, 2212342.
3. A. V. Marenich, C. J. Cramer and D. G. Truhlar, *J. Phys. Chem. B*, 2009, **113**, 6378-6396.
4. T. Lu and Q. Chen, *J. Comput. Chem.*, 2022, **43**, 539-555.
5. G. Kresse and J. Furthmüller, *Phys. Rev. B*, 1996, **54**, 11169-11186.
6. G. Kresse and J. Hafner, *Phys. Rev. B*, 1993, **47**, 558-561.
7. G. Kresse and J. Hafner, *Phys. Rev. B*, 1994, **49**, 14251-14269.
8. L. Giordano, P. Karayaylali, Y. Yu, Y. Katayama, F. Maglia, S. Lux and Y. Shao-Horn, *J. Phys. Chem. Lett.*, 2017, **8**, 3881-3887.
9. W. Wahyudi, X. Guo, V. Ladelta, L. Tsetseris, M. I. Nugraha, Y. Lin, V. Tung, N. Hadjichristidis, Q. Li, K. Xu, J. Ming and T. D. Anthopoulos, *Sci. Adv.*, 2022, **9**, 2202405.
10. A. Fu, J. Lin, Z. Zhang, C. Xu, Y. Zou, C. Liu, P. Yan, D.-Y. Wu, Y. Yang and J. Zheng, *ACS Energy Lett.*, 2022, **7**, 1364-1373.
11. S. Tan, Z. Shadike, J. Z. Li, X. L. Wang, Y. Yang, R. Q. Lin, A. Cresce, J. T. Hu, A. Hunt, I. Waluyo, L. Ma, F. Monaco, P. Cloetens, J. Xiao, Y. J. Liu, X. Q. Yang, K. Xu and E. Y. Hu, *Nat. Energy*, 2022, **7**, 484-494.